Supplementary Materials for

How tropical cyclones drive extreme positive glacier mass balance in the central–eastern Himalayas

Fengying Zhang[a,b], Xuelin Gao[a,b], Shihang Bai[b,e], Ji Zhang[a,b], Jing Gao[c], Rinzin Lhamo[f], Meilin Zhu[b,*], Huabiao Zhao[c,d,*]

[a]College of Earth and Environmental Sciences, Lanzhou University, Lanzhou, 730000, China

[b]Center for the Pan-third Pole Environment, Lanzhou University, Lanzhou, 730000, China

[c]State Key Laboratory of Tibetan Plateau Earth System, Environment and Resources, Institute of Tibetan Plateau Research, Chinese Academy of Sciences, Beijing, 100101, China

[d]Ngari Station for Desert Environment Observation and Research, Institute of Tibetan Plateau Research, Chinese Academy of Sciences, Xizang, 859700, China

[e]College of Atmospheric Science, Lanzhou University, Lanzhou, 730000, China

[f]Xizang Ngari Rutog County Meteorological Bureau, Xizang, 859700, China

Correspondence to Meilin Zhu (zhuml@lzu.edu.cn) and Huabiao Zhao (zhaohb@itpcas.ac.cn)

Contents of this file

Text S1

Figure S1–S13

Table S1–S3

Introduction

We provided the calculation of the cloud cover (C) along with a description of the additional formulas related to the EBFM. Additionally, we included a table of commonly used parameter values.

Supplementary Text S1. Parameterizations used in the energy and mass balance model

A1: Cloud cover

Cloud cover was calculated using the ratio of incoming shortwave radiation (Sin) to the top-of-atmosphere (TOA) radiation (Sedlar and Hock, 2009; Sicart et al., 2006).

$$C = 1 - \left(\frac{S_{in}}{TOA} \right) \tag{1}$$

During nighttime periods, when S_{in} was zero, missing values of C were filled using linear interpolation between the last three hours of the previous day and the first three hours of the following day.

A2: Incoming shortwave radiation (S_{in})

Incoming shortwave radiation is calculated considering the effects of surface slope, aspect, and shading by surrounding terrain as follows:

$$S_{in} = TOAshade \times t_{rg} \times t_w \times t_a \times t_{cl} \tag{2}$$

TOAshade is initially derived by calculating the TOA radiation based on latitude, slope, aspect, and solar geometry. Following Oerlemans (1992), this radiation is then partitioned into direct and diffuse components according to C and topographic shading factors. t_{rg} is the transmissivity for gaseous absorption and scattering, quantifying attenuation due to Rayleigh scattering and ozone absorption based on optical air mass (Atwater and Brown, 1974). t_w is the transmissivity for water vapor absorption, calculated from the dew point temperature and precipitable water content, which are derived from specific humidity and air pressure. t_a is the transmissivity after aerosol absorption, calculated from a simple expression (Houghton, 1954). t_{cl} is the cloud transmissivity, accounting for the nonlinear attenuation effect of C (van Pelt et al., 2012).

$$t_{cl} = 1 - a_2 \times C - b_2 \times C^2 \tag{3}$$

The coefficients a_2 and b_2 were calibrated using observations from automatic weather station 1 (AWS1).

A3: Outgoing shortwave radiation (S_{out})

The S_{out} is calculated based on surface albedo:

$$S_{out} = alb \times S_{in} \tag{4}$$

where *alb* represents the surface albedo.

A4: Albedo

To calculate the reflected shortwave radiation at the glacier surface, a dynamic albedo parameterization scheme was applied, in which surface albedo (*alb*) is expressed as a function of snow aging, melt conditions, snow depth, and interannual climatic variability. To account for the influence of interannual climate variability on snow aging, the positive degree sum (PDS) of each hydrological year was used to modulate the albedo decay timescale. The PDS was calculated over the period from May 1 to September 30. A threshold value of PDS_{th} = 4000 ºC was adopted to distinguish between normal and extreme warm years. The decay timescales were defined as:

$$t_{star} = \begin{cases} t_{wet}, t_{dry}, & PDS < PDS_{th} \\ t_{wetext}, t_{dryext}, & PDS \geq PDS_{th} \end{cases} \tag{5}$$

The ice albedo (a_{ice}) was parameterized as a function of dew point temperature following a formulation similar to Mölg et al (2008). First, an intermediate variable *r* was calculated as:

$$r = \frac{17.271 \times T_a}{237.7 + T_a} + ln\left(\frac{RH}{100}\right) \tag{6}$$

$$T_{dew} = \frac{237.7 \times r}{17.271 - r} \tag{7}$$

The a_{ice} was then computed as:

$$a_{ice} = a_1 \times T_{dew} + b_1 \tag{8}$$

where T_a is air temperature (°C), *RH* is relative humidity (%), and a_1 and b_1 are empirical coefficients. To ensure physical realism, a_{ice} was constrained within the 0.2–0.4. The snow albedo (a_{snow}) was assumed to decay exponentially with snow age:

$$a_{snow} = a_{firn} + \left(a_{snow} - a_{firn}\right) exp\left(-\frac{t}{t_{star}}\right) \tag{9}$$

where a_{firn} is the albedo of firn, and *t* is the snow age. To account for the effect of melt conditions on albedo decay, two different timescales were applied:

$$t_{star} = \begin{cases} t_{wet}, t_{wetext}, & T_s = 0\,^{\circ}C \\ t_{dry}, t_{dryext}, & T_s < 0\,^{\circ}C \end{cases} \tag{10}$$

where T_s is the surface temperature. Snow age was updated based on snowfall events:

$$t = \begin{cases} 0, & P_{snow} \geq P_{th} \\ t+\Delta t, & P_{snow} < P_{th} \end{cases} \tag{11}$$

where P_{snow} is snowfall and P_{th} the snowfall threshold (0.3 mm), and Δt is the model time step. To represent the masking effect of snow cover on underlying ice, a snow–ice transition scheme based on snow depth was applied:

$$alb = a_{snow} + \left(a_{ice} - a_{snow}\right) exp\left(-\frac{h_{snow}}{h^{*}}\right) \tag{12}$$

where h_{snow} is snow depth and h^* is a characteristic depth scale (0.01 m).

A5: Incoming longwave radiation (L_{in}) and outgoing longwave radiation (L_{out})

The parameterization of L_{in} used in this study follows the model of Dilley and O'Brien (1998), combined with the cloud-correction scheme of Sicart et al. (2006) that incorporates relative humidity, as suggested by Zhu et al. (2017). L_{in} is calculated as follows:

$$L_{in} = e \times \sigma \times \left(T_a + 273.15\right)^4 \tag{13}$$

where e is the sky emissivity, and σ is the Stefan-Boltzmann constant (5.67×10^{-8} W m^{-2} K^{-4}).

$$ecs = 1 - \exp\left\{-1.66 * \left[b_1 + b_2 * \frac{\left(T_a + 273.15\right)}{273.16}\right] + b_3 * \sqrt{\left(\frac{w}{25}\right)}\right\} \tag{14}$$

$$e = ecs * \left(b_4 + b_5 * RH + \left(1 - C\right) * b_6\right) \tag{15}$$

b_1, b_2, b_3, b_4, b_5, and b_6 represent empirical constants (Table S2), which were calibrated using in situ observations from AWS2. T_a and RH are air temperature and relative humidity, respectively. The quantity w is the precipitable water (kg m^{-2}), which is estimated using the approach suggested by Prata (1996). L_{out} is calculated based on the Stefan-Boltzmann law, assuming the snow and ice emit as a black body in the infrared.

$$L_{out} = \sigma \times T_s^4 \tag{16}$$

A6: Turbulent heat fluxes

Sensible heat flux (H_{sen}) and latent heat flux (H_{lat}) are calculated following Essery (2004). The calculations are expressed as follows:

$$H_{sen} = Ch \times \rho \times Cp \times u\left(T_a - T_s\right) \tag{17}$$

$$H_{lat} = L_h \times Ch \times \rho \times u \times \left[q_{sat}\left(T_s, P_s\right) - q\right] \tag{18}$$

where Ch is a surface exchange coefficient, ρ is the air density, C_p is the heat capacity of air, u is the wind speed, P_s is the air pressure, and q_{sat} (T_s, P_s) is the saturation specific humidity at T_s and P_s. The latent heat L_h depends on temperature: the latent heat of sublimation (L_s) is used when T_s is below –10 °C, the latent heat of vaporization (L_v) is used when T_s is equal to 0 °C, and a linear interpolation between these two values is applied for intermediate temperatures.

A7: The ground heat flux

The ground heat flux (G) represents the vertical conductive transfer of heat through snow or ice and is calculated following Fourier's law, as the product of an effective thermal conductivity and the temperature gradient. The calculation is expressed as:

$$G = GHF_C \times \left(T_{sub} - T_s\right) \tag{19}$$

where GHF_C is the effective conductivity, a depth-weighted average of the conductivities of the first two subsurface layers that depend on the subsurface depth according to Sturm et al. (1997), and T_{sub} represents the internal snow or ice temperature beneath the surface.

A8: Subsurface model

The evolution of vertical profiles of temperature, density, and water content is simulated using a subsurface model based on the SOMARS model developed by Greuell and Konzelmann (1994). SOMARS has been coupled to a distributed energy balance model in previous studies (Bougamont et al., 2005; Reijmer and Hock, 2008). The subsurface temperature evolution is described by the following thermodynamic equation:

$$\rho_l c_\rho\left(T\right)\frac{\partial T}{\partial t} = \frac{\partial}{\partial z}\left(K(\rho)\right)\frac{\partial T}{\partial z} + \frac{FL_m}{\Delta z} \tag{20}$$

$$K\left(\rho\right) = 0.138 - 1.01\times10^{-3} + 3.23\times10^{-6}\rho_l^2 \tag{21}$$

$$c_\rho\left(T\right) = 152.2 + 7.122T \tag{22}$$

where ρ_l is the layer density, T is the layer temperature, F is the refreezing rate and L_m is the latent heat of melting, z is the layer thickness, $c_\rho(T)$ *is* the heat capacity of snow/ice (Yen, 1981), and $K(\rho)$ is the effective conductivity (Sturm et al., 1997).

Refreezing consists mainly of surface meltwater or rain water:

$$C1 = \frac{c_\rho(T)}{L_M}\int_0^n \rho \Delta T dz \tag{23}$$

$$C2 = \int_0^n \left(1 - \frac{\rho_l}{\rho_{ice}}\right)\rho_{ice} dz \tag{24}$$

$$ref = \begin{cases} \max\left(C2,\ 0\right),\ if\ \ C1 \geq C2 \\ \max\left(C1,\ 0\right),\ if\ \ C1 < C2 \end{cases} \tag{25}$$

where n is the number of layers, ρ_{ice} is the density of the ice, ΔT is the difference between the surface temperature and the layer temperature, and *ref* is the maximum amount of refreezing.

A9: Snowfall (P_{snow})

P_{snow} is calculated by the total daily precipitation (P) and two critical air temperature thresholds for rain (T_{rain}) and snow (T_{snow}). Within the two temperature ranges, P_{snow} was calculated from linear interpolation as the following equation:

$$P_{snow} = \begin{cases} P & T \leq T_{snow} \\ \frac{T_{rain} - T}{T_{rain} - T_{snow}}\ P & T_{snow} < T < T_{rain} \\ 0 & T \geq T_{rain} \end{cases} \tag{26}$$

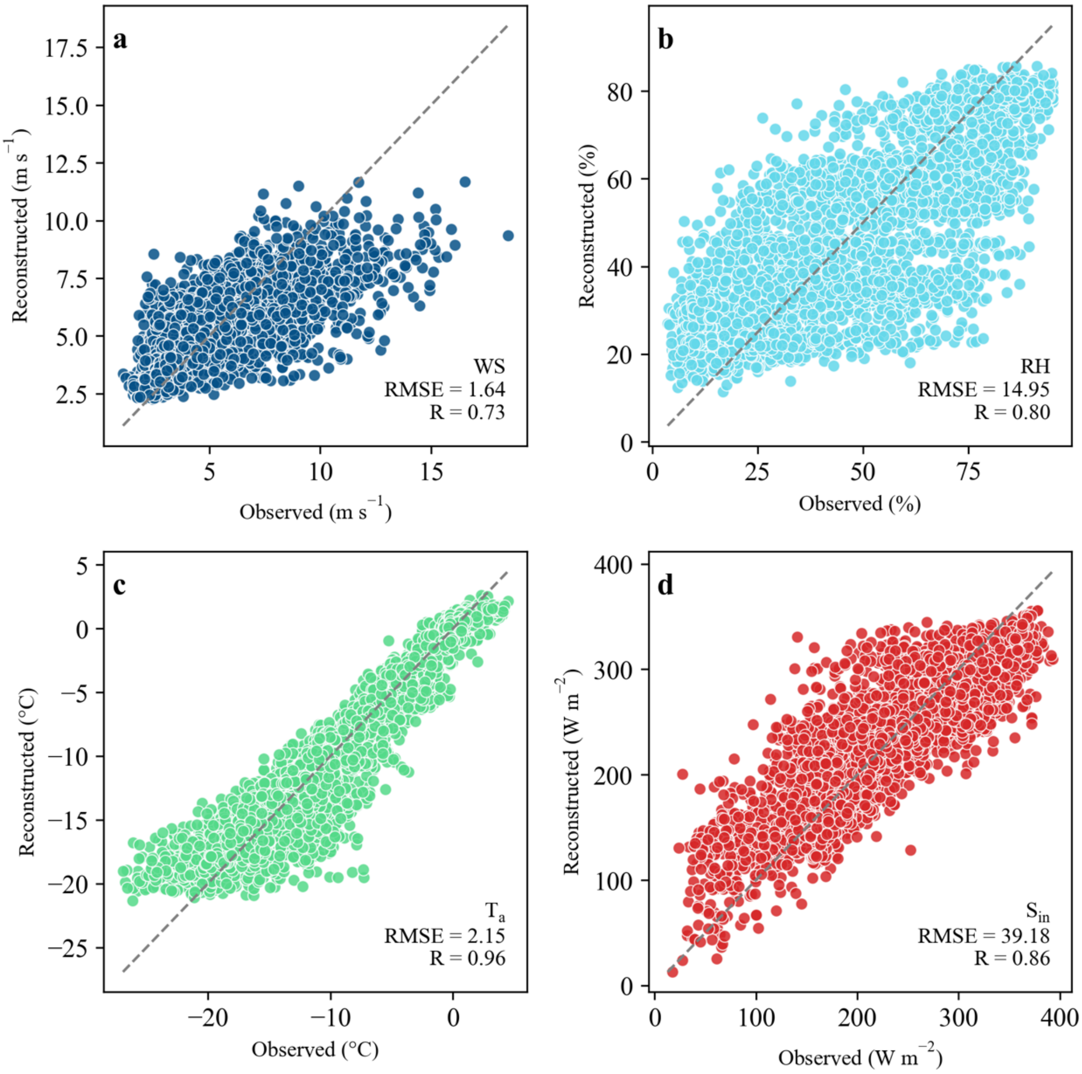

Supplementary Figure. 1. Comparisons between reconstructed and observed meteorological variables at AWS1. (a) air temperature (Ta, ºC), (b) relative humidity (RH, %), (c) wind speed (WS, m s^{-1}), and (d) incoming shortwave radiation (Sin, W m^{-2}).

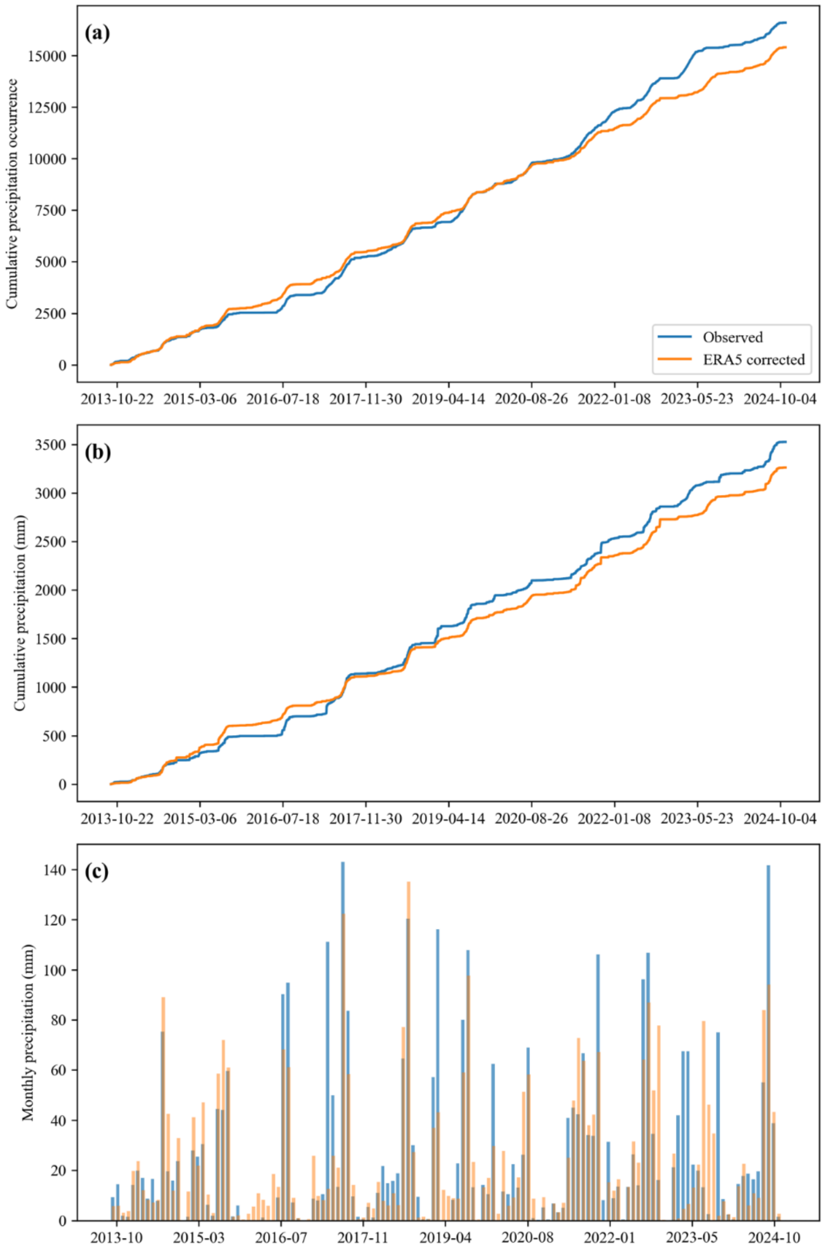

Supplementary Figure. 2. Comparison of (a) cumulative precipitation occurrence, (b) cumulative precipitation amount, and (c) monthly precipitation between the T-200B precipitation gauge and reconstructed precipitation data from ERA5 during the observational period.

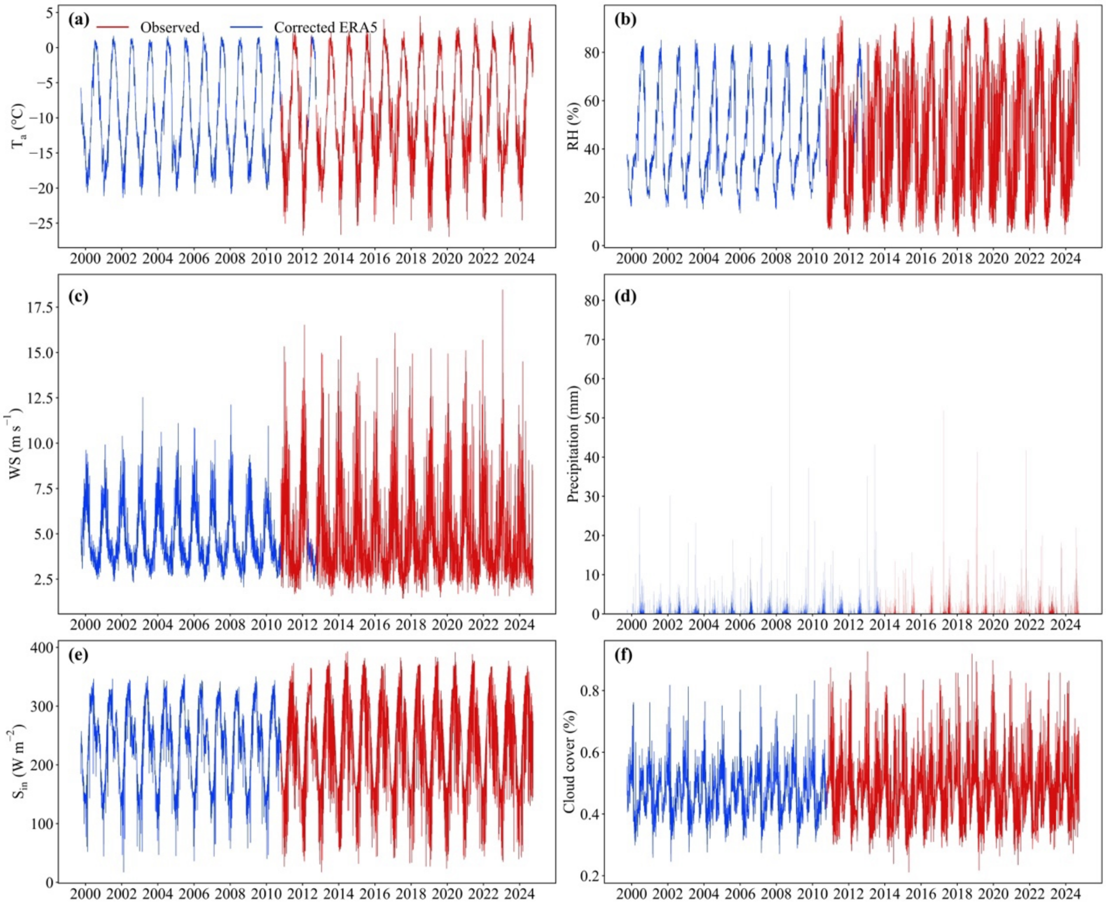

Supplementary Figure. 3. Observed (red) and corrected ERA5 (blue) daily meteorological variables over the period 1999–2024. (a) air temperature (T_a, °C), (b) relative humidity (RH, %), (c) wind speed (WS, m s^{-1}), (d) precipitation (mm), (e) incoming shortwave radiation (S_{in}, W m^{-2}), and (f) cloud cover (%).

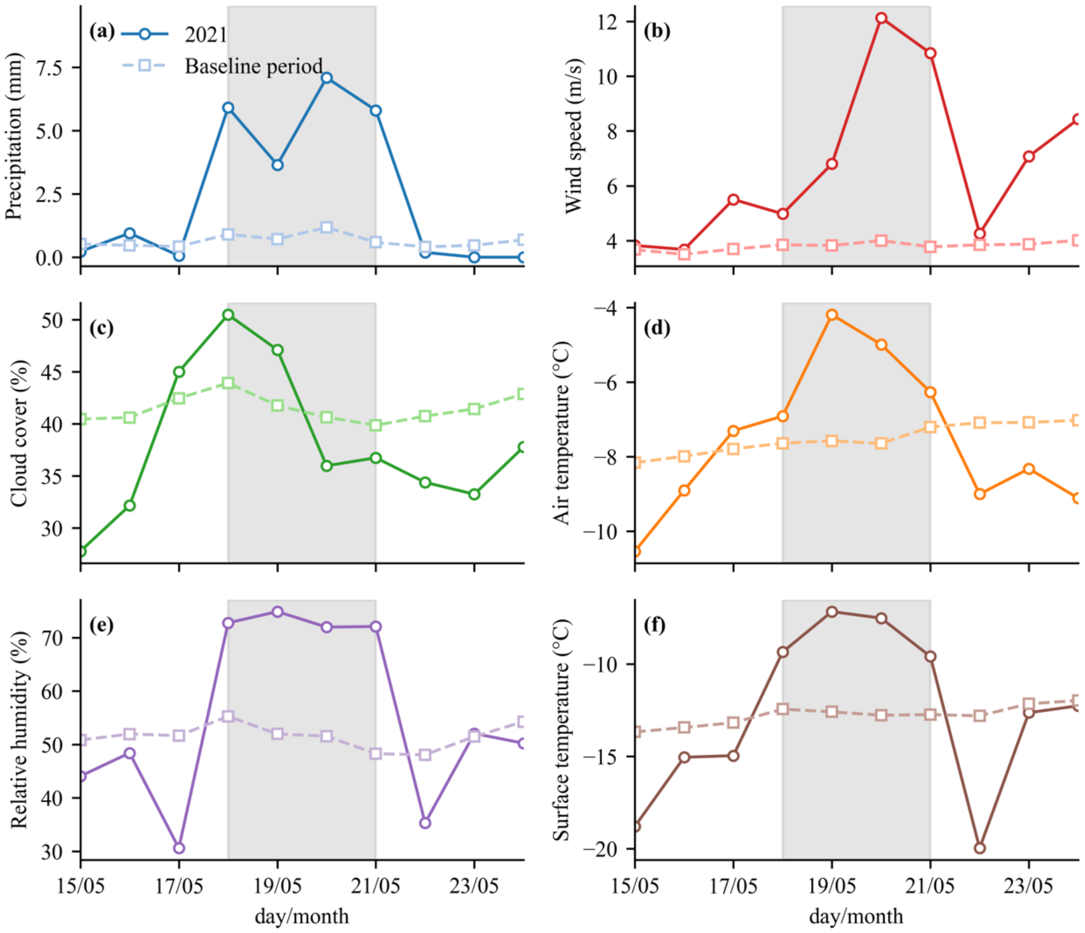

Supplementary Figure. 4. Daily variability of meteorological variables during May 15–23. (a) Precipitation (mm), (b) wind speed (m s^{-1}), (c) cloud cover (%), (d) Air temperature (°C), (e) relative humidity (%) and (f) surface temperature (°C). The solid line with circle markers indicates the values in 2021, while the dashed line with square markers represents the mean of the baseline period (2000–2024).

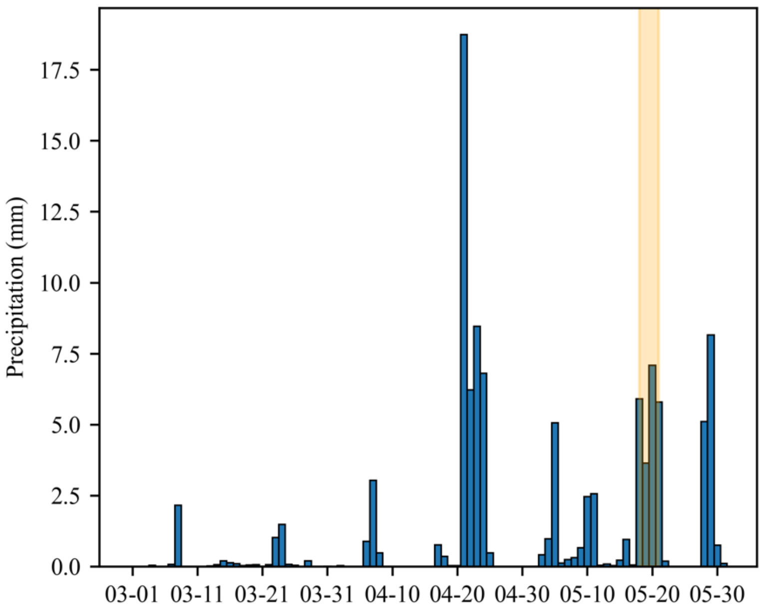

Supplementary Figure. 5. Daily precipitation from March 1–May 30, 2021. The yellow shaded area indicates the TC period.

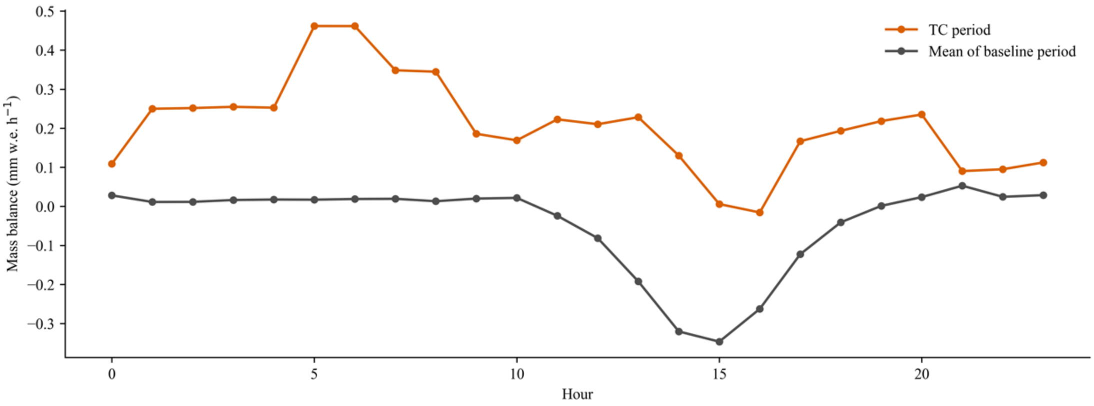

Supplementary Figure. 6. Hourly mass balance variations during the TC period and the baseline period, with orange representing the TC period and black representing the baseline period.

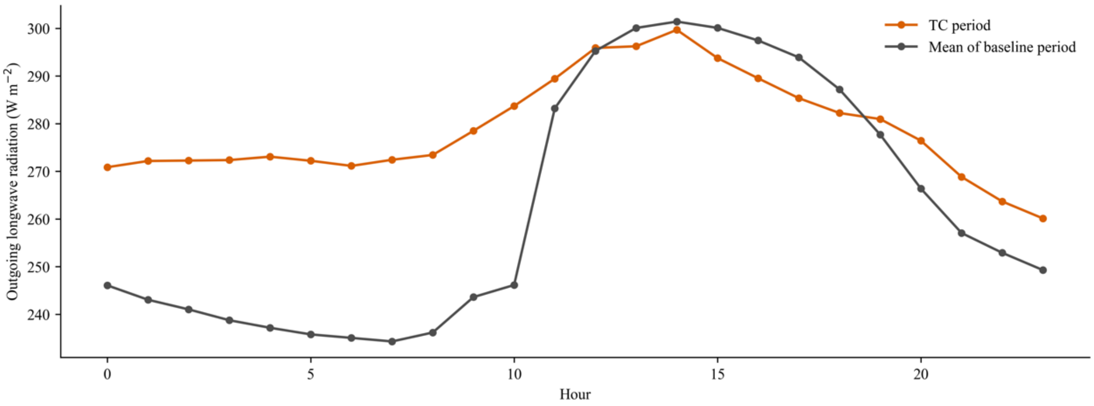

Supplementary Figure. 7. Hourly outgoing longwave radiation (L_{out}, W m^{-2}) during the TC period and the baseline period, with orange representing the TC period and black representing the baseline period.

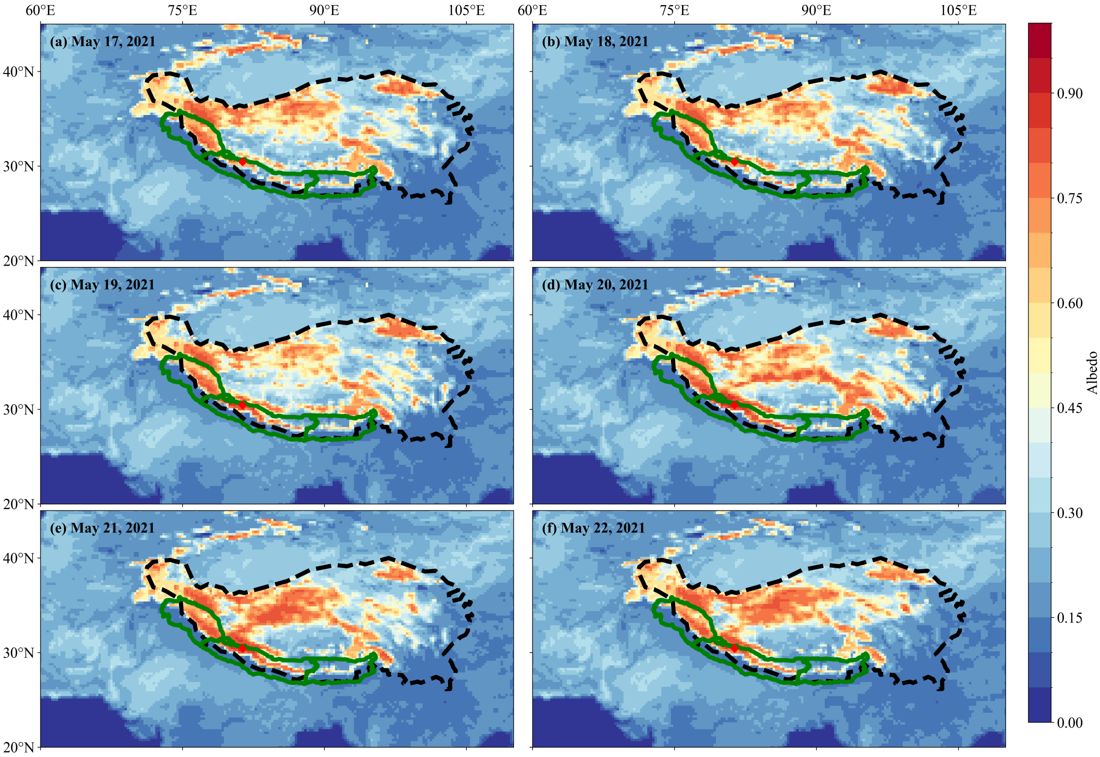

Supplementary Figure. 8. Spatial distribution of daily albedo from ERA5 data over the Tibetan Plateau and surrounding regions from May 17 to 22, 2021. The black dashed line denotes the boundary of the Tibetan Plateau, while the green solid line represents the extent and subdivision of the Himalayas. The red diamond markers indicate the location of Naimona'nyi Glacier. Panels (a)–(f) correspond to May 17–22, 2021, respectively.

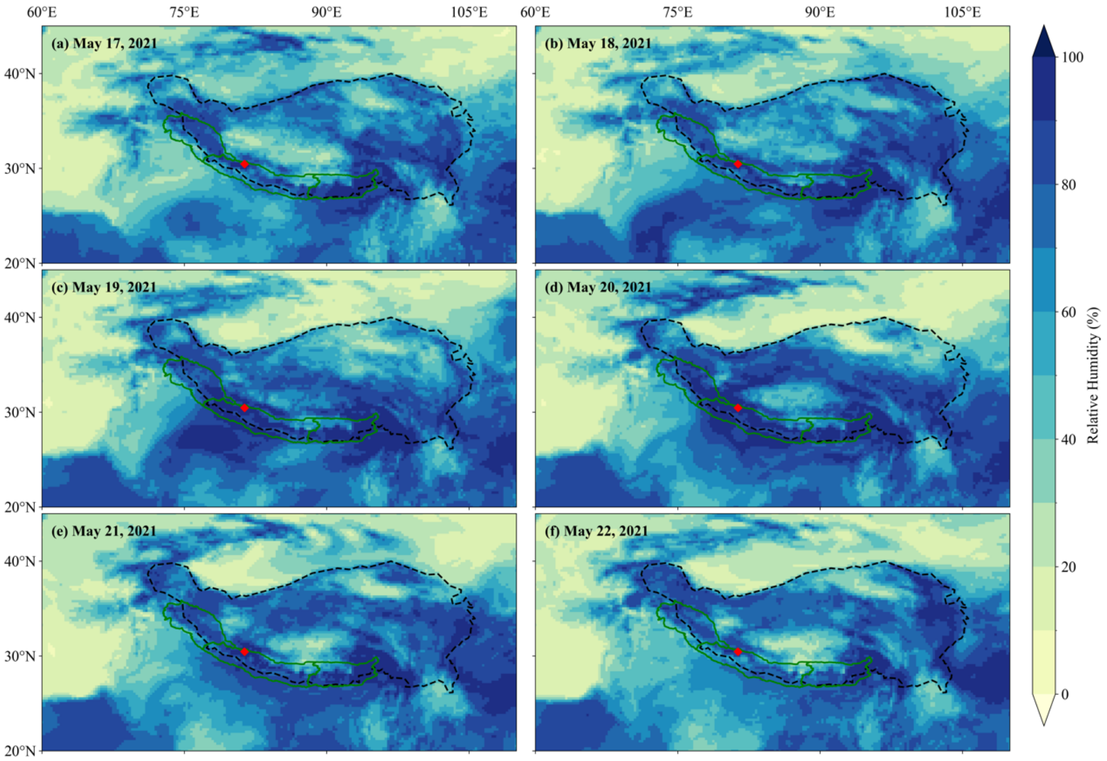

Supplementary Figure. 9. Spatial distribution of daily mean relative humidity from ERA5 reanalysis data over the Tibetan Plateau and surrounding regions from May 17 to 22, 2021. The black dashed line denotes the boundary of the Tibetan Plateau, while the green solid line represents the extent and subdivision of the Himalayas. The red diamond markers indicate the location of Naimona'nyi Glacier. Panels (a)–(f) correspond to May 17–22, 2021, respectively.

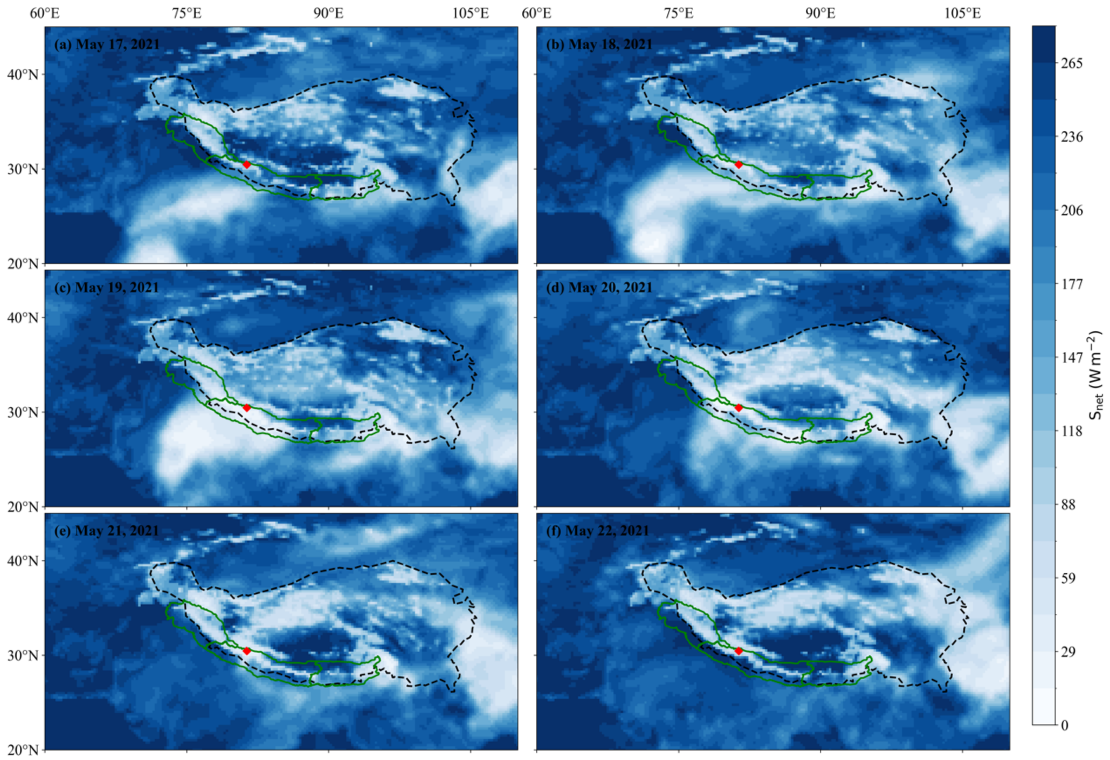

Supplementary Figure. 10. Spatial distribution of daily net shortwave radiation from ERA5 reanalysis data over the Tibetan Plateau and surrounding regions from May 17–22, 2021. The black dashed line denotes the boundary of the Tibetan Plateau, while the green solid line represents the extent and subdivision of the Himalayas. The red diamond markers indicate the location of Naimona'nyi Glacier. Panels (a)–(f) correspond to May 17–22, 2021, respectively.

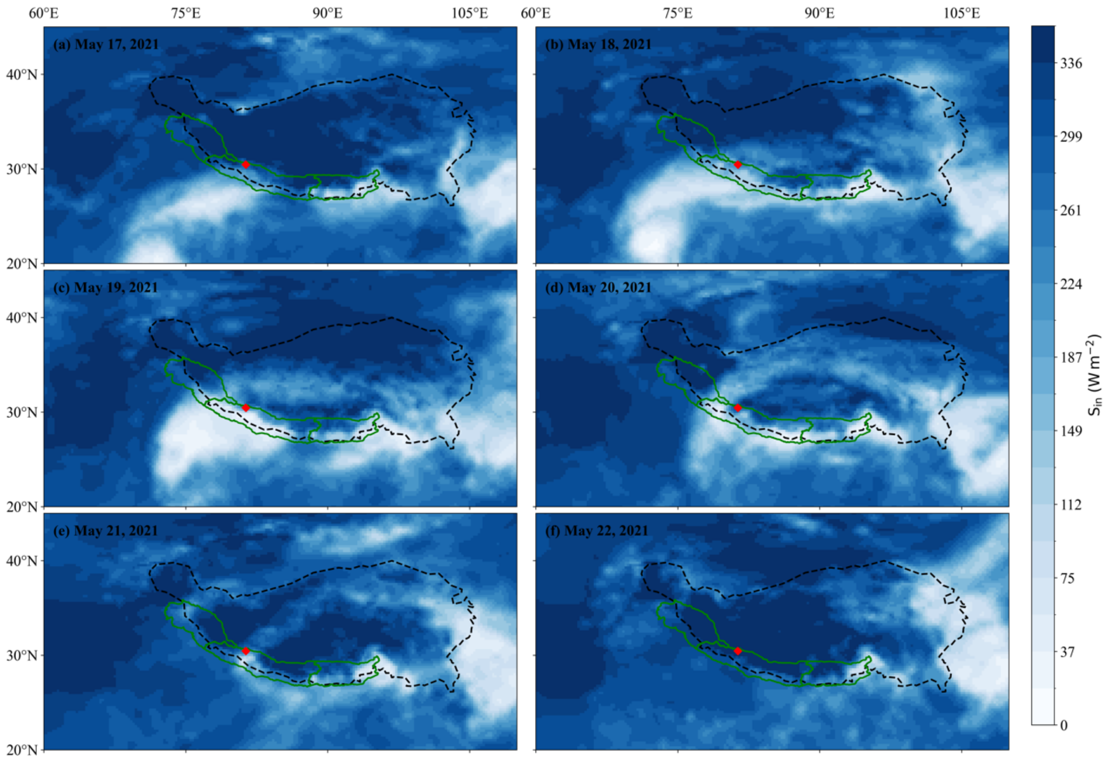

Supplementary Figure. 11. Spatial distribution of daily incoming shortwave radiation (S_{in}) from ERA5 reanalysis data over the Tibetan Plateau and surrounding regions from May 17–22, 2021. The black dashed line denotes the boundary of the Tibetan Plateau, while the green solid line represents the extent and subdivision of the Himalayas. The red diamond markers indicate the location of Naimona'nyi Glacier. Panels (a)–(f) correspond to May 17–22, 2021, respectively.

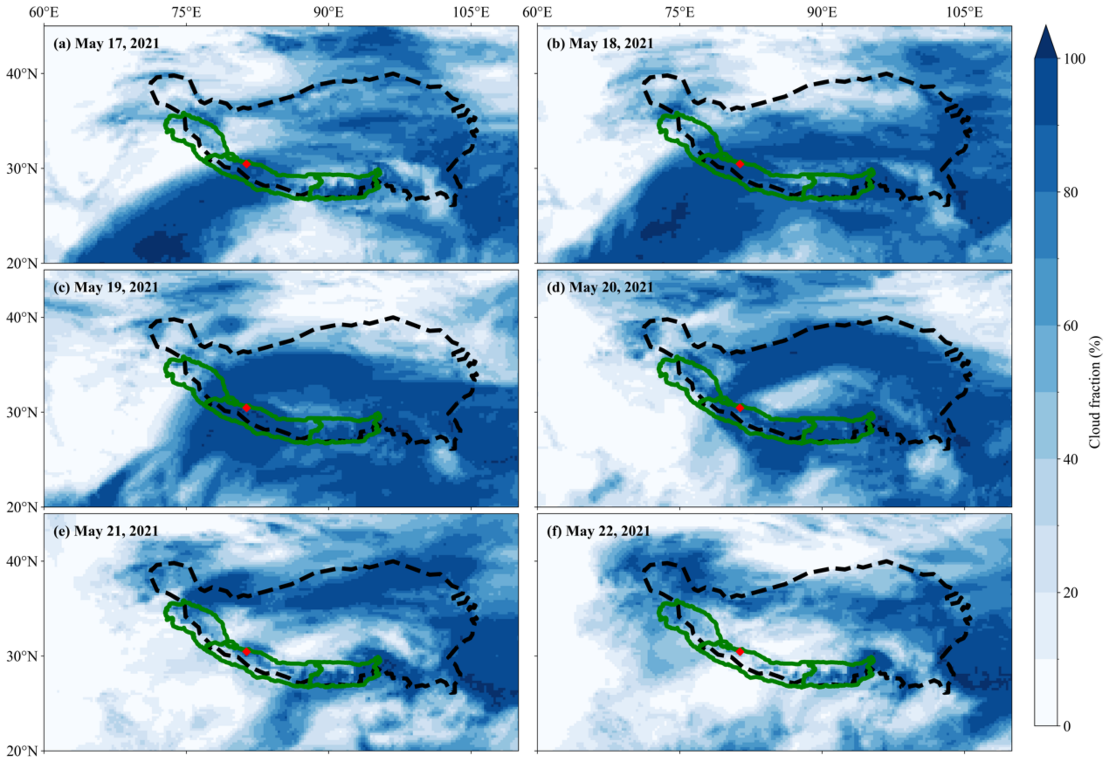

Supplementary Figure. 12. Spatial distribution of cloud fraction from ERA5 reanalysis data over the Tibetan Plateau and surrounding regions from May 17–22, 2021. The black dashed line denotes the boundary of the Tibetan Plateau, while the green solid line represents the extent and subdivision of the Himalayas. The red diamond markers indicate the location of Naimona'nyi Glacier. Panels (a)–(f) correspond to May 17–22, 2021, respectively.

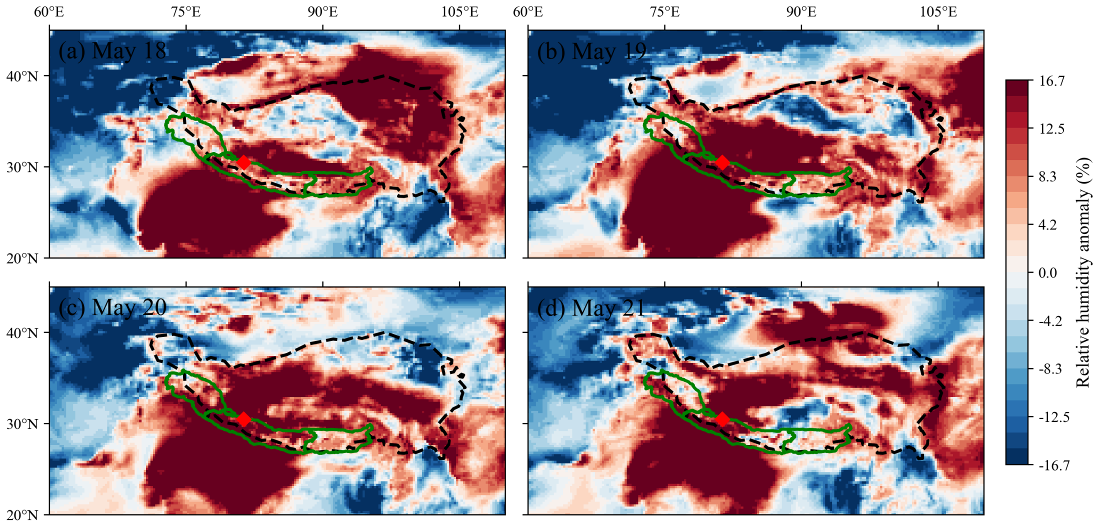

Supplementary Figure. 13. Spatial distribution of daily relative humidity anomalies over the Tibetan Plateau during May 18–21, 2021. Panels (a–d) correspond to May 18, May 19, May 20, and May 21, respectively. The black dashed line outlines the Tibetan Plateau boundary, while the green solid line indicates the extent and sub-regions of the Himalayas. Red diamonds mark the location of Naimona'nyi Glacier. Anomalies are defined relative to the 2000–2024 climatological mean for the corresponding day of the year.

Table S1. Characteristics of the sensors installed in the eddy covariance system for measuring turbulent fluxes and meteorological variables in this study.

Parameters	Sensors	Accuracy	Height (m)	Location
T_a	Vaisala HMP 45C	±0.2°C (–40 to +60°C)	2.5	AWS2 and AWS3
	Campbell CS215	±0.4ºC (5 to 40ºC), ±0.9ºC (–40 to +40ºC)	3	AWS1
	Hobo MX2301	±0.2ºC (0 to 70ºC), ±0.25ºC (–40 to 0ºC)	2.2	T1, T2, T3, T4, and T5
RH	Vaisala HMP 45C	±2.5% (0–100%)	2.5	AWS2 and AWS3
	Campbell CS215	±5% (<10% or >90%)	3	AWS1
	Hobo MX2301	±2% (10–90%) ±4% (0–100%)	2.2	T1, T2, T3, T4, and T5
WS	Young 05103 wind monitor	±0.3 m/s	3	AWS1 and AWS2
P	T-200B	±0.1 mm	1.5	AWS1
S_{in}	LICOR LI200X Silicon Pyranometer	±5% (–40 to +65°C)	2.5	AWS1
	Campbell CS300	5% for daily totals	2.5	AWS1
S_{in} *and* S_{out}	Huxeflux NR01	±1.8%	2	AWS2 and AWS3
L_{in} *and* L_{out}		±7%	2	
Press	Vaisala PTB210	±0.35 hPa	1.2	AWS2
CO_2 and H_2O	Li-7500 open-path CO_2/H_2O analyzer	<1% (-25 to +50°C)	2.5	AWS3
u' *and* v'	WindMaster Pro	10 mm s^{-1} (0−65 m s^{-1})	2.5	AWS3
w'				
T'		1 mm s^{-1}		

0.01°C (−40°C to +50°C)

Table S2. Input Parameters for the EBFM Model.

Abbreviation	Parameter	Values
T_{rate1}	vertical air temperature gradient (ºC 100m-1) above 5919	-0.69
T_{rate2}	vertical air temperature gradient (ºC 100m^{-1}) below 5919	-0.84
P_{rate1}	vertical precipitation gradient (% m^{-1}) above 5800m	0.086
P_{rate2}	vertical precipitation gradient (% m^{-1}) below 5800m	0.02
$T_{rainsnow}$	temperature of snow to rain transition (K)	274.15
alb_{snow}	fresh snow albedo	0.85
alb_{firn}	firn albedo	0.55
t_{wet}	albedo time scale when surface temperature equal to 0	14
t_{dry}	albedo time scale when surface temperature smaller than 0	18
t_{wetext}	albedo time scale for wet snow (T_s = 0 °C) under extreme climate conditions.	3.9
t_{dryext}	albedo time scale for dry snow (T_s < 0 °C) under extreme climate conditions.	8
a	Parameter for Ice albedo model	–0.0253
b	Parameter for Ice albedo model	0.2577
b_1–b_6	parameters of L_{in} model	–0.39, 0.938, 1.168, 0.752, 0.0031, –0.086
z0	bulk coefficient of turbulent heat flux (m)	0.0004

Table S3. Free parameters in the energy and mass balance model and their range and the optimal values.

Symbol	Parameter	Values	Range used for uncertainty estimation	Mean mass balance sensitivity (m w.e. day^{-1})	
				Baseline period	2021 TC period
$a_{freshsnow}$	Fresh snow albedo	0.85	±10%	0. 32	0. 35
a_{firn}	Firn albedo	0.55	±10%	0.38	0.01
t_{wet}	Albedo time scale when surface temperature equal to 0	14	±10%	0.02	0
t_{dry}	Albedo time scale when surface temperature smaller than 0	18	±10%	0	0
a	Parameter for Ice albedo model	–0.0253	±10%	0	0
b	Parameter for Ice albedo model	0.2577	±10%	0	0
ΔP_1	Vertical precipitation gradient above 5800 m a.s.l.	8.6% 100 m^{-1}	±10%	0. 01	0. 03
ΔP_2	Vertical precipitation gradient above 5800 m a.s.l.	2% 100 m^{-1}	±10%	0. 01	0. 03
$T_{snow/rain}$	Phase threshold for snow/rain	1 °C	±10%	0. 02	0
z_0	Roughness length of turbulent heat flux	0.0004 m	±10%	0	0. 01
	Total uncertainty			0. 16	0.11

References

Atwater, M.A., Brown, P.S., 1974. Numerical Computations of the Latitudinal Variation of Solar Radiation for an Atmosphere of Varying Opacity. Journal of Applied Meteorology (1962-1982) 13, 289–297. https://www.jstor.org/stable/26176296

Bougamont, M., Bamber, J.L., Greuell, W., 2005. A surface mass balance model for the Greenland Ice Sheet. Journal of Geophysical Research: Earth Surface 110. https://doi.org/10.1029/2005JF000348

Dilley, A. C., and D. M. O'Brien, 1998: Estimating downward clear sky long-wave irradiance at the surface from screen temperature and precipitable water. Quart. J. Roy. Meteor. Soc., 124, 1391–1401, doi:10.1002/qj.49712454903.

Essery, R., Etchevers, P., 2004. Parameter sensitivity in simulations of snowmelt. Journal of Geophysical Research: Atmospheres 109. https://doi.org/10.1029/2004JD005036

Greuell, W., Konzelmann, T., 1994. Numerical modelling of the energy balance and the englacial temperature of the Greenland Ice Sheet. Calculations for the ETH-Camp location (West Greenland, 1155 m a.s.l.). Global and Planetary Change, Greenland ice margin experiment (GIMEx) 9, 91–114. https://doi.org/10.1016/0921-8181(94)90010-8

Houghton, H.G., 1954. ON THE ANNUAL HEAT BALANCE OF THE NORTHERN HEMISPHERE. Journal of the Atmospheric Sciences 11, 1–9. https://doi.org/10.1175/1520-0469(1954)011%253C0001:OTAHBO%253E2.0.CO;2

Mölg, T., Cullen, N.J., Hardy, D.R., Kaser, G., Klok, L., 2008. Mass balance of a slope glacier on Kilimanjaro and its sensitivity to climate. International Journal of Climatology 28, 881–892. https://doi.org/10.1002/joc.1589

Oerlemans, J., 1992. Climate sensitivity of glaciers in southern Norway: application of an energy-balance model to Nigardsbreen, Hellstugubreen and Alfotbreen. Journal of Glaciology 38, 223–232. https://doi.org/10.3189/S0022143000003634

Prata, A. J., 1996: A new, long-wave formula for estimating downward clear-sky radiation at the surface. Quart. J. Roy. Meteor. Soc., 122, 1127–1151, doi:10.1002/qj.49712253306.

Reijmer, C.H., Hock, R., 2008. Internal accumulation on Storglaciären, Sweden, in a multi-layer snow model coupled to a distributed energy- and mass-balance model. Journal of Glaciology

54, 61–72. https://doi.org/10.3189/002214308784409161

Sedlar, J., Hock, R., 2009. Testing longwave radiation parameterizations under clear and overcast skies at Storglaciären, Sweden. The Cryosphere 3, 75–84. https://doi.org/10.5194/tc-3-75-2009

Sicart, J.E., Pomeroy, J.W., Essery, R.L.H., Bewley, D., 2006. Incoming longwave radiation to melting snow: observations, sensitivity and estimation in Northern environments. Hydrological Processes 20, 3697–3708. https://doi.org/10.1002/hyp.6383

Sturm, M., Holmgren, J., König, M., Morris, K., 1997. The thermal conductivity of seasonal snow. Journal of Glaciology 43, 26–41. https://doi.org/10.3189/S0022143000002781

van Pelt, W.J.J., Oerlemans, J., Reijmer, C.H., Pohjola, V.A., Pettersson, R., van Angelen, J.H., 2012. Simulating melt, runoff and refreezing on Nordenskiöldbreen, Svalbard, using a coupled snow and energy balance model. The Cryosphere 6, 641–659. https://doi.org/10.5194/tc-6-641-2012

Yen, Y.-C., 1981. Review of Thermal Properties of Snow, Ice, and Sea Ice. U.S. Army, Corps of Engineers, Cold Regions Research and Engineering Laboratory.

Zhu, M., Yao, T., Yang, W., Xu, B., & Wang, X. 2017. Evaluation of parameterizations of incoming longwave radiation in the high-mountain region of the Tibetan Plateau. Journal of Applied Meteorology and Climatology, 56(4), 833-848.